Catalytic thermal decomposition of residual solvent on ZnO promotes defect-driven visible-light photocatalysis: mechanistic insights from multiscale spectroscopy

Antoine Farcy [1*], Julien G. Mahy [1], Sofie Cambré[2], Henk Schut[3], Eduard Fron[4], Sophie Hermans [5], Stéphanie D. Lambert[1]

[1] Department of Chemical Engineering – Nanomaterials, Catalysis & Electrochemistry, University of Liège, B6a, Quartier Agora, Allée du six Août 11, 4000 Liège, Belgium

[2] Theory and Spectroscopy of Molecules and Materials, TSM[2], Department of Physics, University of Antwerp, Universiteitsplein 1, Antwerp B-2610, Belgium

[3] Delft University of Technology, faculty of Applied Sciences, Department of Radiation Science and Technology, Mekelweg 15, 2629 JB Delft, The Netherlands.

[4] Core Facility for Advanced Spectroscopy Leuven, KU Leuven, Celestijnenlaan 200F, 3000 Leuven, Belgium;

[5] Institute of Condensed Matter and Nanosciences - Molecular Chemistry, Materials and Catalysis (IMCN/MOST), Université catholique de Louvain (UCLouvain), Place Louis Pasteur 1, Box L4.01.03, 1348 Louvain-La-Neuve, Belgium

*Corresponding author: Antoine Farcy; email: antoine.farcy@uliege.be

Abstract

Defect engineering is a powerful strategy to activate wide-bandgap semiconductors, yet controlling the formation of specific vacancies remains challenging. Here, we introduce a general, solvent-directed approach to engineer defects, demonstrated with ZnO. By selecting methanol as the synthesis solvent and performing thermal annealing under nitrogen, the in-situ decomposition of the

solvent generates a local reductive environment that selectively creates zinc vacancies (V_{Zn}). These vacancies, absent in ethanol-derived ZnO, enable sub-bandgap absorption and improved charge separation, leading to enhanced visible-light photocatalytic activity. While solvent effects on morphology and defect populations have been occasionally noted, leveraging the catalytic decomposition of the solvent itself as a design principle for controlled, vacancy-centered defect formation has not, to our knowledge, been demonstrated. Comprehensive spectroscopic analyses, including steady-state and time-resolved photoluminescence, steady-state and time-resolved electron paramagnetic resonance, and positron annihilation spectroscopy, elucidate the nature, dynamics, and photoactivity of these vacancies. Under visible-light irradiation ($\lambda > 395$ nm), methanol-derived ZnO achieves up to a twofold increase in p-nitrophenol degradation compared to untreated samples. This work establishes a simple, dopant-free, and scalable route to defect engineering via solvent selection, offering a broadly applicable strategy for activating wide-bandgap semiconductors under visible light.

1. Introduction

Engineering specific defects in wide-bandgap semiconductors is a powerful strategy to extend their photoresponse into the visible range, yet controlling the formation of such vacancies in a safe, scalable, and reproducible manner remains challenging. Zinc oxide (ZnO) is a low-toxicity, abundant semiconductor with promising photocatalytic properties [1–6]; however, its wide bandgap (≈3.3-3.4 eV) limits activation to ultraviolet light, restricting practical applications under solar irradiation [1,7].

Intrinsic defects in zinc oxide (ZnO) are central to its optical, electronic, and catalytic properties, with oxygen vacancies (V_O) and zinc vacancies (V_{Zn}) being the most common and functionally significant [8–12]. V_O are often associated with sub-bandgap absorption and influence charge carrier recombination, but their role is relatively well understood and easier to generate [13]. In contrast, V_{Zn} are less prevalent yet critically important as they act as electron traps, stabilize photogenerated charges, and prolong hole lifetimes, thereby enhancing hole-mediated oxidative reactions that are crucial for efficient visible-light photocatalysis[4,12–14] .

Controlling the formation of V_{Zn}, however, remains a major challenge, as it requires precise manipulation of local redox conditions without introducing unwanted impurities[13]. Various strategies have been explored to generate V_{Zn}, including high-temperature annealing in reducing atmospheres such as H_2 or Ar/H_2 mixtures, chemical reduction using strong reducing agents such as $NaBH_4$, hydrogen plasma treatment, and multi-step post-synthesis treatments [15–17].

While these approaches can successfully create zinc vacancies, they often involve hazardous reagents, complex procedures, and provide limited control over defect type, concentration, and spatial distribution, which can compromise reproducibility and scalability. To clearly disentangle solvent-driven effects from purely thermal or atmospheric contributions, a reference ZnO sample synthesized in water was also investigated throughout this study. Here, we present an exceptionally simple, green, and compact approach to selectively generate V_{Zn} in ZnO by leveraging the catalytic decomposition of

the synthesis solvent itself. During thermal annealing under nitrogen, methanol undergoes in-situ decomposition at the ZnO surface, producing CO and H_2, which create a local reducing environment that stabilizes zinc vacancies without the need for any external dopants or hazardous chemicals. Ethanol, by contrast, does not produce comparable defects under identical conditions, highlighting the critical role of solvent choice. By combining multi-technique characterization, including electron paramagnetic resonance (EPR), time-resolved EPR (TREPR), positron annihilation spectroscopy (PAS), and time-resolved photoluminescence (TRPL), with photocatalytic degradation of p-nitrophenol (PNP) and ibuprofen (IBU) under visible light, we demonstrate that this solvent-directed defect engineering effectively enhances charge separation and prolongs hole lifetimes, resulting in significantly improved photocatalytic performance. This work establishes a dopant-free, scalable, and environmentally friendly strategy for defect engineering in wide-bandgap semiconductors, showing that the synthesis solvent itself can serve as a functional design element for controlling intrinsic defects and activating semiconductors under visible-light irradiation.

2. Materials and methods

2.1 Synthesis of photocatalysts

2.1.1 ZnO A

5.9 g of zinc acetate dihydrate ($Zn(CH_3COO)_2.2H_2O$, VWR CHEMICALS) was dissolved in 250 mL of methanol at 60 °C under stirring. At the same time, 3.6 g of potassium hydroxide (KOH, VWR CHEMICALS) was dissolved in 130 mL of methanol at room temperature after which this solution was heated to 60 °C. After, the KOH was added dropwise into the zinc acetate solution at 60°C and the mixture was kept under agitation for 1 h. After the reaction, the solid formed in suspension was filtered, then washed with methanol and dried into an oven for 12 h at 100 °C.

2.1.2 ZnO B

The same procedure was followed for the synthesis of ZnO B but ethanol is used as solvent instead of methanol. The sample was also washed several times with ethanol and dried.

2.1.3 ZnO C

As a control, the same procedure was done with water instead of methanol or ethanol to synthesize the ZnO which is labelled ZnO C.

2.1.4 Calcination

The effect of calcination was also tested. First of all, a thermal treatment at 500 °C under nitrogen atmosphere during 2 h was done for both samples, referred to as ZnO A-N_2, ZnO B-N_2 and ZnO C-N_2. Additionally, thermal treatment under air in the same conditions was done for the ZnO A, referred to as ZnO A-Air.

2.2 Samples characterization

Crystallite structure and phases are determined using a Bruker D8 Twin-Twin X-Ray diffractometer with Cu-Kα radiation of 1.54 Å in a range between 2 θ = 10° to 70°. Crystallite size within the different samples is estimated using the Scherrer formula [18]

$$d = \frac{K\lambda}{\beta \cos(\theta)} \quad (1)$$

where K is a shape factor (0.9), λ is the X-Ray wavelength (1.54 Å), β is the full width half maximum and θ is the Bragg angle.

Nitrogen adsorption-desorption isotherms are collected on a micromeritics ASAP 2420 at a temperature of - 196 °C. Before measurements, samples are degassed under high vacuum at 80 °C for 15 h. The specific surface area (S_{BET}) is determined using the Brunauer Emmett and Teller (BET) equation by taking the relative pressure data between 0.05 and 0.25.

Morphologies of powders are obtained by Scanning Electron Microscopy (SEM) on a TESCAN CLARA device from Bruker operating at 15 keV. The samples, previously dispersed in acetone using an ultrasonic bath for 2 min are placed on a glass slide. The surface is coated with gold before being introduced in the microscope.

Diffuse reflectance (DRS) measurements are performed using a PerkinElmer Lambda1050 UV-vis-NIR spectrophotometer equipped with a Spectralon-coated integrating sphere with PMT (photomultiplier) and InGaAs detectors. The spectra are transformed using the Kubelka–Munk function to produce a signal, normalized for comparison between samples, enabling the band gaps to be calculated. The details of this treatment method are described elsewhere [19].

Steady-state photoluminescence experiments were acquired with an FLS-1000 spectrometer from Edinburgh Instruments, equipped with a 450 W Xenon lamp as excitation source, passing through a double monochromator with spectral band width of 1 nm. The PL is detected through a single monochromator and a UV-visible photomultiplier with thermoelectric cooling (200 – 980 nm, PMT-

980). Emission spectra were collected with a spectral band width of 5 nm, an integration time per pixel of 0.5 s, and using a dedicated powder sample holder with additional long-pass filters to reduce the detection of scattered stray light. Spectra were automatically corrected for the dark counts (background) and sensitivity of the detectors. When additional long-pass filters were used, spectra were afterwards corrected with the transmission spectra of these filters.

EPR was performed with a high-Q cylindrical TE011 resonator (ER4122SHQE) in a standard X-band spectrometer (Bruker Elexys-II E500, 9.85 GHz). Approximately 20mg of the ZnO powder was added inside a 3 mm quartz tube and EPR experiments were conducted at room temperature with a magnetic-field modulation amplitude of 0.1 mT and a microwave power of 20 mW. This microwave power was chosen to avoid microwave saturation of any of the signals. All spectra were recorded with the same integration time and afterwards corrected for small deviations for the weight of the sample. Samples were illuminated in situ (cavity with optical access) using a 447nm laser with 100 mW excitation power (measured just in front of the cavity).

Zeta potential and hydrodynamic diameter measurements were performed on the various sols using a DelsaNano C instrument (Beckman Coulter) to assess colloidal stability. Prior to measurement, all samples were sonicated for 10 minutes to ensure optimal dispersion.

Nanosecond Time-resolved Luminescence: A 360 nm laser pulse (8 ns, 10 Hz) generated by a system consisting of a pulsed Nd:YAG laser (Quanta-Ray INDI-40, Spectra Physics) was used to excite the samples. The excitation light was focused on the sample by a 150-mm focal length lens and a small part of this light was sent to a fast photodiode to generate a trigger signal. Right angle configuration between excitation and light collection paths was used and the luminescence was collected, filtered and focused on the entrance slit of a 30 cm focal length monochromator. A SpectroPro-300i monochromator/spectrograph was used to disperse the emitted light and select the desired wavelength. The optical signal was detected by a PMT (Hamamatsu, R928) and the transient electrical signal was amplified and sent to a computer-controlled oscilloscope. A homemade Labview based

software was used to control and trigger the instruments, read, average, and store the transient data. The samples were placed in a 1-mm thick cuvette. The experiments have been performed in one time window of 20 ns.

Doppler broadening measurements were performed using the Delft Variable Energy Positron beam (VEP), a mono-energetic, magnetically guided beam delivering 10^4 positrons per second with tunable energies ranging from 1 to 25 keV, thus allowing depth-resolved defect analysis over a range of approximately 0 to 2 micrometres.

2.3 Photocatalytic experiments

The photocatalytic activity of the five ZnO samples was assessed by monitoring the degradation of *p*-nitrophenol (PNP) under visible-light irradiation ($\lambda > 395$ nm). Each catalyst (5 mg) was dispersed in 5 mL of 10^{-4} M PNP aqueous solution, yielding a final catalyst concentration of 10 g/L. The dispersions were magnetically stirred and placed in individual quartz tubes arranged symmetrically around a 230 W halogen lamp (emission: 300–800 nm). To restrict illumination to the visible range, all tubes were covered with optical long-pass filters cutting wavelengths below 395 nm. A water-cooling system was used to maintain constant temperature during illumination.

Dark controls were prepared in parallel to evaluate adsorption effects, and a blank (PNP solution without catalyst) was included to assess potential photolysis. After 24 h of irradiation, 1 mL aliquots were sampled, filtered through 0.2 µm PP membranes to remove particles, and acidified with one drop of 0.01 M HCl to ensure full protonation of PNP. The absorbance was measured at 317 nm, corresponding to the maximum of the acidic form, using a Genesys 150 UV-Vis spectrophotometer (Thermo Scientific). Quantification was based on a previously established calibration curve. All experiments were performed in triplicate to ensure reproducibility.

To evaluate the generality of the photocatalytic behavior, ibuprofen was selected as a representative pharmaceutical pollutant. For each material, 50 mL of an aqueous ibuprofen solution (initial concentration: 52 mg L^{-1}) was placed in a flat petri dish (8.5 cm diameter), with a photocatalyst loading of 10 g L^{-1}. Prior to irradiation, the suspensions were magnetically stirred in the dark for 30 min to establish adsorption-desorption equilibrium. Visible-light irradiation was then applied for 24 h, while maintaining the reactor temperature at 25 ± 2 °C. Mineralization was further evaluated by total organic carbon (TOC) analysis.

Finally, scavenger experiments were performed only for p-nitrophenol to identify the dominant reactive species. Ammonium oxalate (AO) and isopropanol were used as hole and hydroxyl radical scavengers, respectively, at a concentration of 0.05 mM in 50 mL of aqueous PNP solution. After 24 h of visible-light irradiation, the remaining PNP concentration was quantified by UV–Vis spectroscopy at 317 nm.

3. Results and discussion

3.1 Characterizations

3.1.1 Composition, morphology, and texture of the ZnO nanoparticles samples

The X-ray diffraction (XRD) patterns shown in Figure 1 confirm the formation of ZnO with the wurtzite crystal structure for all samples, regardless of the solvent used (methanol, ethanol or water). The first two diffractograms (black and red), corresponding to ZnO A and ZnO A-N_2 respectively, show a noticeable narrowing of the diffraction peaks after nitrogen annealing. This decrease in full width at half maximum (FWHM) suggests an increase in crystallite size.

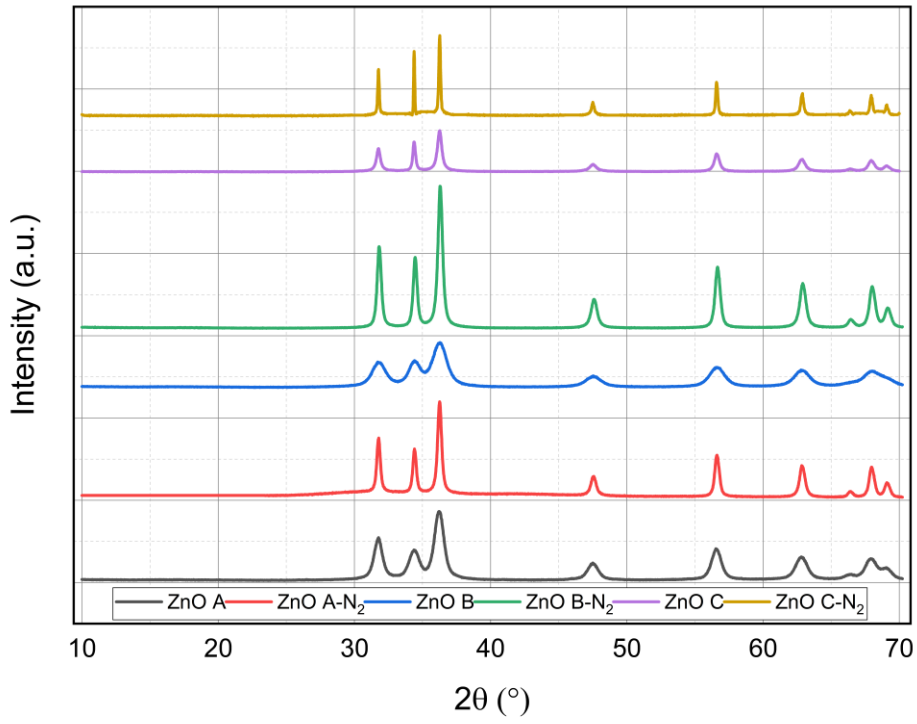

Figure 1 - XRD patterns of the different zinc oxides : ZnO A in black, ZnO A-N_2 in red, ZnO B in blue, ZnO B-N_2 in green, ZnO C in purple and ZnO C-N_2 in yellow.

Using the Scherrer equation (Equation 1), the average crystallite size is estimated to increase from 11 nm to 24 nm following thermal treatment at 500 °C for 2 h. Similarly, the XRD patterns of ZnO B and

ZnO B-N_2 indicate crystallite sizes ranging from 8 nm to 21 nm. The same trend is shown for the ZnO C. The narrowing of the XRD peaks observed after nitrogen annealing is attributed to the thermally induced growth of ZnO crystallites and the relaxation of lattice microstrain. Annealing at 500 °C promotes particle sintering, which increases the average crystallite size (from 11 to 24 nm for ZnO A and from 9 to 22 nm for ZnO B, Table 1). At the same time, thermal treatment reduces structural disorder, which in turn decreases microstrain broadening within the wurtzite lattice [20].

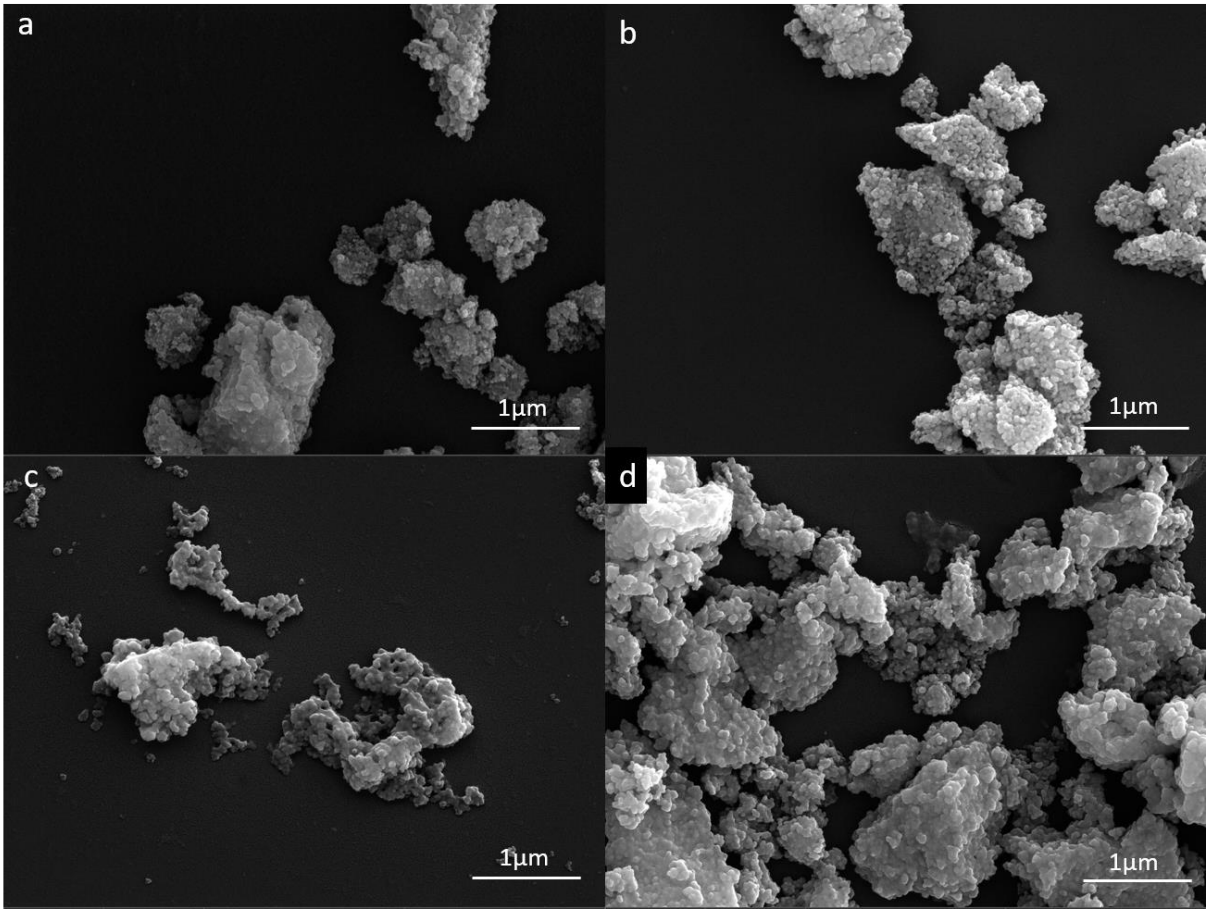

Figure 2 - SEM images of the four samples at a 50.000 times magnification : (a) ZnO A, (b) ZnO A-N_2, (c) ZnO B, (d) ZnO B-N_2

SEM images reveal that both ZnO A (Figure 2a) and ZnO B (Figure 2c) consist of small, spherical nanoparticles that tend to aggregate into larger clusters, even before thermal treatment. This

morphological behavior is corroborated by dynamic light scattering (DLS) measurements (Table 1), which show that ZnO A exhibits the smallest hydrodynamic radius, followed by ZnO B. Upon thermal treatment at 500 °C for 2 h, ZnO A-N_2 shows a more granular structure than ZnO A, which is not the case for ZnO B-N_2 compared to ZnO B. DLS experiments show an approximately twofold increase in hydrodynamic radius for ZnO A-N_2 and ZnO B-N_2, compared to their untreated counterparts. Consistent with this observation, surface area measurements reveal a significant reduction in specific surface area after annealing: from 80 m^2/g to 50 m^2/g for ZnO A, and from 90 m^2/g to 60 m^2/g for ZnO B. These trends align well with the increase in crystallite size determined from XRD (Table 1), confirming the sintering and particle growth induced by thermal treatment.

X-ray photoelectron spectroscopy (XPS) measurements were also performed to probe the chemical states of Zn and O. No significant differences were observed among the samples, for brevity, the corresponding spectra are not shown. This is consistent with the expectation that the solvent-induced modifications primarily affect the near-surface region of the ZnO particles, whereas XPS probes a depth of 5-10 nm. The enhancement in photocatalytic activity, a surface-driven process, further supports that the observed defect formation and charge separation improvements occur predominantly at or near the particle surface, explaining why XPS do not reveal substantial changes.

Table 1 a - Table showing the various results of the characterizations carried out (to be added): S_{BET} corresponds to the specific surface area measurement (m^2/g); D_{XRD} refers to the crystallite size (nm); D_{DLS} to the hydrodynamic radius (µm); and E_g to the band gap energy (eV).

Sample	S_{BET} (m^2/g)	D_{XRD} (nm)	D_{DLS} (µm)	$E_{g,direct}$ (eV)
ZnO A	80	11	1.6	3.26
ZnO A-N_2	50	24	4.2	3.21
ZnO B	90	9	2	3.29
ZnO B-N_2	60	22	4.3	3.22

3.1.2 Further insight in the mechanisms with spectroscopic studies

To elucidate the formation of zinc vacancies induced by methanol decomposition and their effect on charge carrier dynamics, we employed multi-technique characterization, using visible-light photocatalysis as a functional probe. First, steady-state photoluminescence (PL) spectra were recorded under 320 nm excitation (3.875 eV), well above the ZnO bandgap (Figure 3a-c), to probe all electronic states, including deep-level defects. The emission spectra were limited to sub-bandgap energies, confirming their defect-related origin. All samples exhibited broad emission bands centered at 600 nm in the as-synthesized state, which redshifted to 650 nm after thermal treatment, reflecting modifications in the defect landscape and the formation or redistribution of deeper traps.

Assuming comparable electron-hole recombination dynamics, the observed PL intensity can be qualitatively related to the number of radiative defects. Notably, ZnO B showed an overall PL intensity 1.2 times higher than ZnO A, indicating a greater population of radiative defects. Thermal treatments led to a strong reduction in PL intensity, particularly for ZnO B. Annealing under nitrogen caused only a slight redshift, whereas air treatment induced a more pronounced redshift, suggesting differences in defect stabilization.

To better resolve defects relevant to visible-light-driven processes, PL spectra were also collected under selective 447 nm excitation (Figure 3c), directly probing sub-bandgap transitions associated with solvent-induced defects. For as-synthesized ZnO A and B, emission is dominated by a peak at 525 nm, with secondary features at 650 nm and 750 nm. After N_2 annealing, ZnO A showed complete suppression of the 525 nm peak, leaving only the 750 nm emission, consistent with the formation of deeper, methanol-induced zinc vacancies. In contrast, ZnO B-N_2 retained a dominant 650 nm feature, resembling ZnO A-Air, highlighting the critical role of methanol in directing the formation of V_{Zn} and modifying the defect landscape to favor visible-light activity.

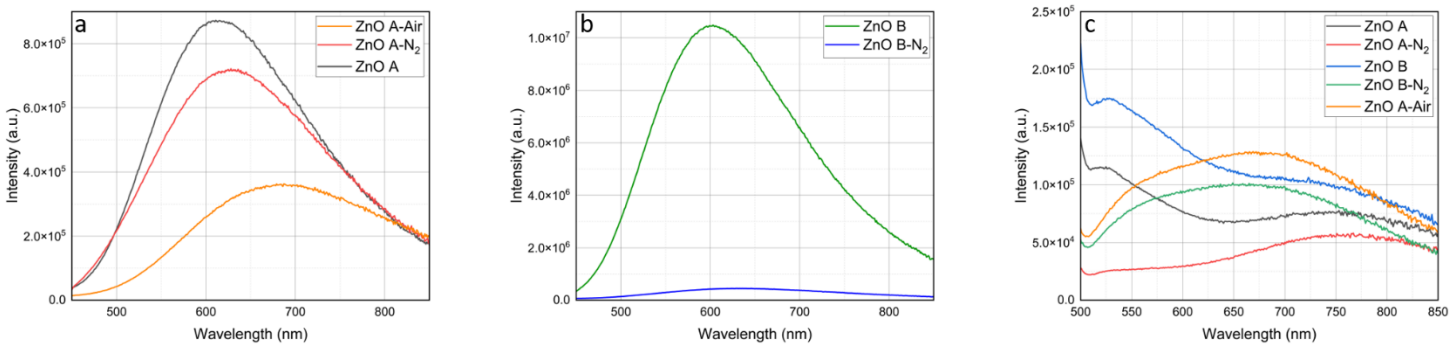

Figure *3* - PL spectra collected by illuminating the samples at λ_{exc} = 320 nm for (a) & (b). Panel (c) displays the spectra for an excitation wavelength of λ_{exc} = 447 nm. Note the varying intensity scale due to differences in emission quantum yield.

To evaluate whether these changes reflect alterations in the band gap of ZnO, diffuse reflectance spectroscopy (DRS) was performed (Figure 4). A small but consistent redshift in the absorption edge is observed upon N_2 and air annealing: from 3.26 to 3.22 eV and 3.24 eV in ZnO A and from 3.29 to 3.22 eV in ZnO B. These shifts point to slight bandgap narrowing, likely resulting from defect-induced band tailing or local structural relaxation. These subtle changes cannot explain the marked differences observed in the PL spectra, therefore further investigation was performed via time-resolved photoluminescence and EPR.

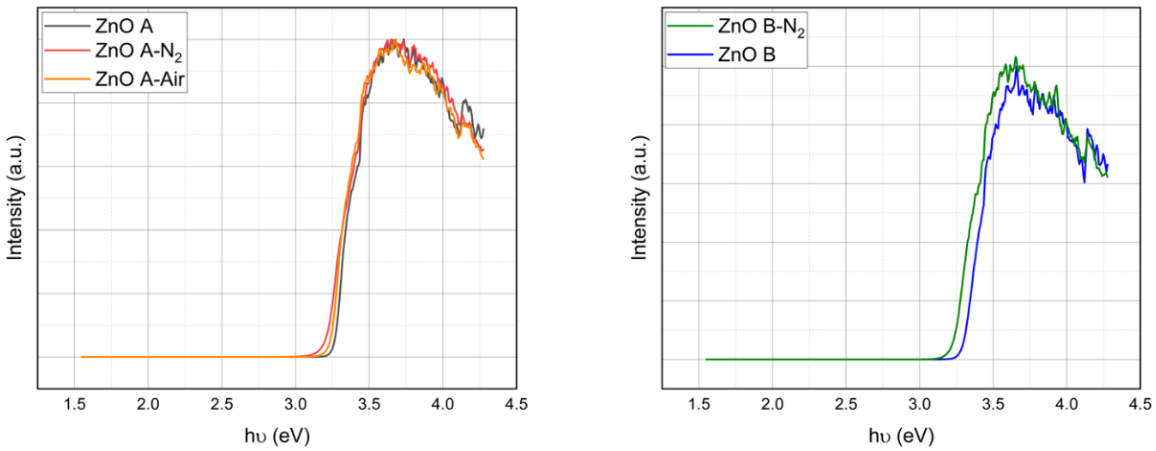

Figure 4 - DRS Spectra for, on the left, ZnO A and ZnO-N_2. On the right, ZnO B and ZnO B-N_2

Time-resolved photoluminescence (TRPL) measurements were performed (Figure 5) using time-correlated single photon counting. While excitation at 447 nm was initially attempted to selectively probe sub-bandgap defect states, the signal-to-noise ratio was insufficient due to long acquisition times. Therefore, excitation at 360 nm, above the ZnO bandgap, was employed to monitor emission at 550 nm associated with defect-related transitions. Excitation at this higher energy allows carriers to access a broader range of defect levels, including deep traps that may not be directly excitable at 447 nm, providing a more complete view of the defect landscape generated by the solvent. Since all samples were measured under identical conditions, the relative variations in lifetimes reliably reflect differences in defect-assisted charge trapping and recombination, giving meaningful insight into the impact of methanol-induced vacancies on charge dynamics.

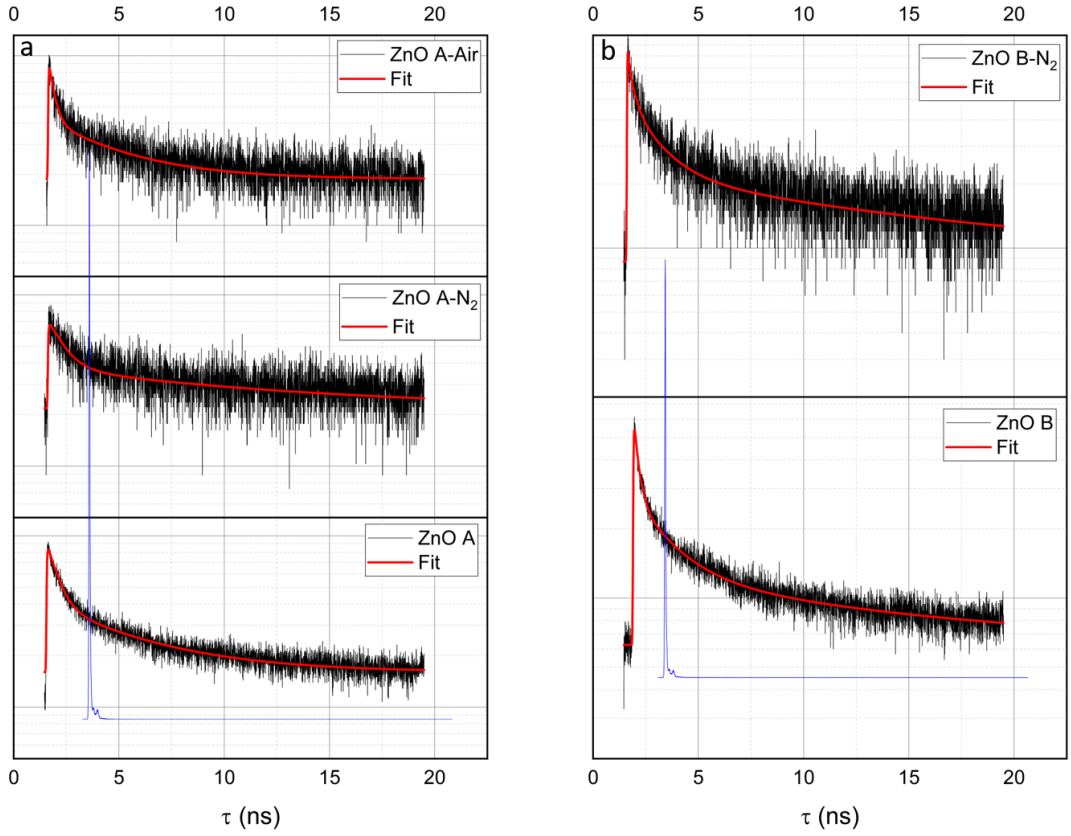

Figure 5 – Time-Resolved Photoluminescence spectra recorded with a lambda-exc = 340 nm. the detector is set to 550 nm nm (2 nm spectral bandwidth). In blue, the Instrument Response Function (IRF). On the left (a), ZnO A and on the right (b), ZnO B.

At 550 nm, the pristine ZnO synthesized in methanol (ZnO A) exhibited biexponential decay kinetics with characteristic lifetimes of τ_1 = 0.47 ns and τ_2 = 4.48 ns. Upon thermal treatment under N_2, these lifetimes increased substantially (τ_1 = 0.70 ns, τ_2 = 11.07 ns), indicative of reduced non-radiative recombination and prolonged charge separation, consistent with the stabilization of methanol-induced zinc vacancies. In contrast, air-treated ZnO A displayed shortened lifetimes (τ_1 = 0.22 ns, τ_2 = 3.50 ns), reflecting defect passivation and rapid carrier recombination.

ZnO synthesized in ethanol (ZnO B) showed triexponential decay kinetics with τ_1 = 0.19 ns, τ_2 = 1.76 ns, and τ_3 = 12.08 ns, indicative of a distinct defect landscape. Post-N_2 treatment led to increases in τ_1 and τ_3 (τ_1 = 1.4 ns, τ_3 = 14.53 ns), suggesting that thermal activation under inert atmosphere also promotes defect stabilization and charge separation, though less efficiently than in methanol-derived ZnO.

To further probe the sub-bandgap defects revealed by TRPL, conventional and light-induced EPR spectroscopy were performed. EPR selectively detects paramagnetic centers such as singly ionized oxygen vacancies (V_O^+) and zinc vacancies (V_{Zn}), both critical for charge trapping. In the dark, ZnO A exhibited a weak signal at g = 1.96 (359 mT), attributed to V_O^+ centers. Illumination at 447 nm increased this signal nearly fiftyfold (Figure 6a), confirming efficient photo-trapping of electrons.

For ZnO A-N_2, a second signal at g = 2.00 (352 mT) emerged (Figure 6b), attributed to zinc vacancies formed under the local reducing conditions created by methanol decomposition. As a reference, ZnO treated with $NaBH_4$ (at 500 °C under nitrogen as well) also exhibits an EPR signal at g = 2.00, confirming that this resonance corresponds to V_{Zn} centers (Figure 7f). The V_O^+ signal at g = 1.96 displayed increased asymmetry, while no significant light-induced intensity change was observed, suggesting that these deep zinc vacancies are either not directly addressable at 447 nm.

Annealing in air resulted in an almost silent EPR spectrum, with only weak, non-light-responsive features near g = 1.96, consistent with PL results showing reduced 447 nm emission and indicating that few defect states remain optically active.

ZnO B behaved differently, the as-prepared sample showed negligible dark EPR signal, with illumination revealing a weak g = 1.96 resonance, indicating lower V_O^+ concentration than in ZnO A. N_2 annealing modestly increased this signal, yet no g = 2.00 resonance appeared, confirming that ethanol favors oxygen vacancies but does not induce zinc deficiency due to its limited reductive decomposition.

Finally, neither ZnO C nor ZnO C-N_2, synthesized using water as solvent, exhibited any detectable paramagnetic signal under dark conditions. This absence of EPR-active centers indicates that, in the absence of alcohol-derived surface species, thermal treatment under nitrogen does not promote the formation or stabilization of optically addressable defects in ZnO.

This control experiment confirms that the emergence of paramagnetic V_O^+ and, more critically, V_{Zn} centers is not a generic consequence of annealing atmosphere, but rather arises from solvent-assisted surface chemistry specific to alcohol-based syntheses, and in particular to methanol.

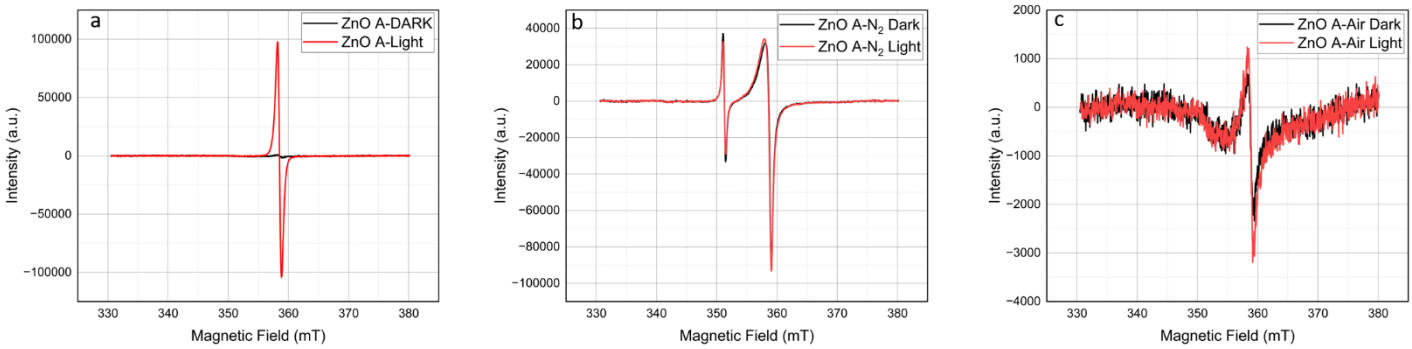

Figure 6 - EPR spectra for ZnO A samples without (*black*) and with light illumination at 447 nm (*red)*

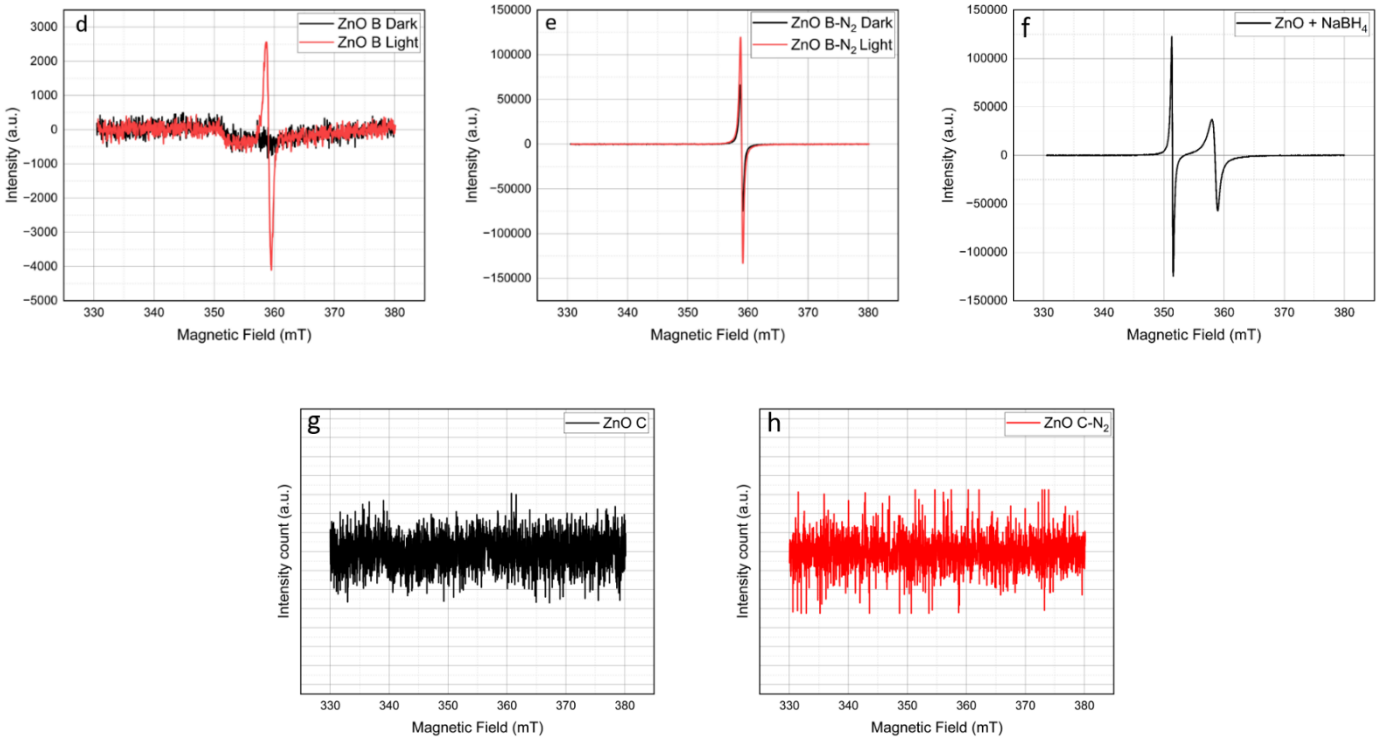

Figure 7 - EPR spectra for ZnO B samples without (dark) and with light illumination at 447 nm (red). Figure 7f : ZnO + $NaBH_4$. Figure 7 g : ZnO C and Figure 7 h : ZnO C-N_2. The EPR spectra for ZnO C and ZnO C-N_2 were recorded under dark conditions.

To clarify the photophysical origin of the photocatalytic differences, time-resolved EPR spectroscopy was conducted (Figure 8). As shown previously, steady-state EPR spectra of ZnO exhibit two resonances near 352 mT and 359 mT. The 359 mT line, if present, remains stable under illumination, whereas the 359 mT signal is markedly enhanced for ZnO A and ZnO B, but only weakly for the other samples. This suggests differing mechanisms for the photo-trapped electrons.

In TREPR, the 359 mT signal was monitored during light on/off cycles at 447 nm (2.77 eV), which selectively excites sub-bandgap defect states, consistent with PL emission profiles. Based on [21], a kinetic model was used to fit the EPR transients, where photoexcited electrons are either trapped directly into deep, EPR-active states (rate constant k_1), or hop through shallower traps before eventual deep trapping (k_2). The model yields biexponential growth kinetics during illumination:

$$y(t) = y_0 + C_1 \cdot \left(1 - e^{\{-k_1 t\}}\right) + C_2 \cdot \left(1 - e^{\{-k_2 t\}}\right) \qquad (2)$$

With $y_0$the offset at time t=0. C_1 and C_2 are parameters that describe which process is dominant and k_1 and k_2 are parameters that describe the timescales of the two processes.

A larger value of *k* means a faster trapping. The fit of the experimental data shows that the slow component (k_2) related to the hopping-dependent trapping is in most cases very similar and in the range of 2-5 ms^{-1} (Table 1), while the fast component (direct trapping) is very different for the different samples, being absent in ZnO A-Air and ZnO A-N_2, and significantly present in ZnO A with a value of k_1 = 25.5 ms^{-1} and in ZnO B and ZnO B-N_2 with a value of k_1 = 63.5 and 70.07 ms^{-1} respectively, therefore resulting in a large effect on the EPR signal upon illumination. This might point at specific deep traps not being present or at a much lower concentration in the ZnO A-Air and ZnO-N_2 samples, in agreement with the PL resutls which show reduced emission for these samples (and a disappearance of specific bands when excited at 447 nm).

When the illumination is stopped, the recombination and detrapping kinetics can be studied, both occuring on different timescales. For ZnO A-Air, ZnO A-N_2 and ZnO B-N_2 a single exponential can fit the data very well, while for the other two samples both a fast and a slower kinetics is observed. Therefore we use the following model:

$$C_3 e^{\{-k_3 t\}} + C_4 e^{\{-k_4 t\}} \qquad (3)$$

C_3 and C_4 are, as well, parameters that describe which process is dominant and k_3 and k_4 are parameters that describe the timescales of the detrapping/recombination process.

The lower k_1 constant for ZnO A (25.5 ms^{-1}) means that the trapping time is slower than for ZnO B (65 ms^{-1}) and ZnO B-N_2 (70 ms^{-1})

For the constants k_3 and k_4, that of ZnO A is lower at 5 ms^{-1} compared with 7ms^{-1} for ZnO B, showing that release of unpaired electrons is slower for ZnO A than for ZnO B. However, the signal remains permanently present over the measured timescale for ZnO B-N_2, meaning that the electron is still trapped and not released.

The spectroscopic data also clarify the complementary role of oxygen vacancies (V_O) and zinc vacancies (V_{Zn}) in charge separation. V_O create defect states nearer the conduction band, enabling fast trapping of photogenerated electrons, as reflected in the TREPR. V_{Zn}, in contrast, correspond to deeper acceptor-like states located nearer to the valence band. In ZnO A-N_2, where both defects coexist, electrons initially trapped in V_O can further relax into V_{Zn}, forming a cascade of defect states that stabilizes electrons and suppresses direct electron-hole recombination. This interpretation is consistent with the longer TRPL lifetimes and the persistent EPR signal at g ≈ 2.00. Such a dual-defect landscape effectively enhances charge separation, explaining why ZnO A-N_2 outperforms samples containing only V_O.

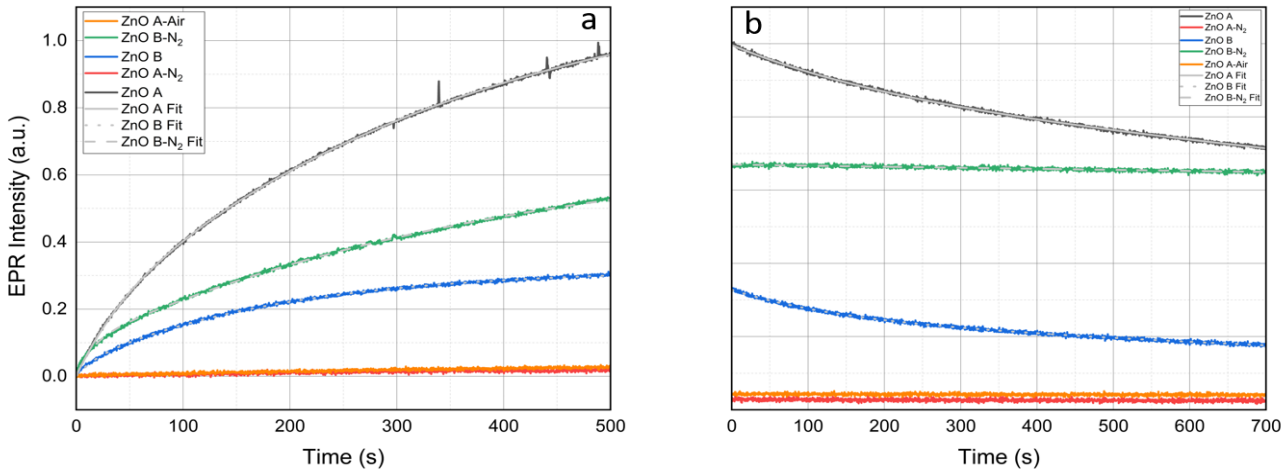

Figure 8 – TREPR experiments: (a) rise of the EPR signal upon light excitation (light on at t=0s) showing different growth rates for the different samples. (b) decrease of the EPR signals after shutting down the times, showing different detrapping rates for the charges.

Table 1 b - Table summarizing the results of the different characterizations performed: EPR refers to electron paramagnetic resonance; TREPR corresponds to time-resolved electron paramagnetic resonance under light-on conditions (k_1 and k_2 relate to charge trapping kinetics) and light-off conditions (k_3 and k_4 relate to detrapping or recombination kinetics); TRPL denotes time-resolved photoluminescence, providing information on the different charge carrier recombination times

Sample	EPR V_O	EPR V_{Zn}	**TREPR (light ON)**			**TREPR (light OFF)**			**TRPL at 550 nm** τ_1 **(ns)** τ_2 **(ns)** τ_3 **(ns)**
			k_1 **(ms^{-1})**	k_2 **(ms^{-1})**	C_1 C_2	k_3 **(ms^{-1})**	k_4 **(ms^{-1})**	C_3 C_4	
ZnO A	Yes	No	25.5 ± 0.9	2.84 ± 0.04	0.15 1.06	0.298 ± 0.003	5.038 ± 0.1	0.87 0.12	0.47±0.034 4.48±0.13 /
ZnO A-N_2	Yes	Yes	/	3.0 ± 0.3	/ 0 .023	0.19 ± 0.01	/	0.03 /	0.72±0.09 11.08±2.58 /
ZnO A-Air	Less	No	/	2.5 ± 0.2	/ 0.037	0.083 ± 0.006	/	0.043 /	0.23±0.02 3.53±0.18 /
ZnO B	No	No	64 ± 5	5.30 ± 0.05	0.036 0.28	0.51 ± 0.006	7.17 ± 0.13	0.25 0.3	0.19±0.01 1.76±0.1 12.08±0.74
ZnO B-N_2	Yes	No	70 ± 3	2.50 ± 0.03	0.093 0.60	0.043 ±0.008	/	0.67 /	1.4±0.2 0.22±0.70 14.53±1.75

Finally, positron annihilation techniques have been employed for nearly five decades as highly sensitive probes to investigate voids and open volumes in condensed matter, by measuring the local electron density distribution[22]. When positrons with controlled energies are implanted into a solid, they thermalize and diffuse until annihilation occurs with an electron, resulting, most often, in the emission of two 511 keV gamma photons in opposite directions. The energy distribution of these gamma rays is broadened due to the momentum of the annihilating positron-electron pair, a phenomenon known as Doppler broadening. This effect provides insight into the electronic environment at the annihilation site. The energy spectrum near 511 keV is typically characterized by two parameters: the S-parameter, which reflects annihilations with low-momentum valence or free electrons and is sensitive to defect concentration (the most important parameter for photocatalysis); and the W-parameter, associated with high-momentum core electrons, offering information about the chemical surroundings of the defects. Positron interactions in solids involve various complex processes such as backscattering, thermalization, diffusion, surface interactions, and defect trapping. These interactions enable the detection of a wide range of defects, including vacancies, dislocations, voids, interfaces, precipitates, and grain boundaries.

In the following, we focus on the S parameter, as it directly reflects the surface electron density, while the corresponding W parameter is shown for completeness. PAS further supports the defect-rich surface of ZnO A and ZnO A-N_2, which display higher S parameters at the surface (0.54) relative to ZnO B (0.52), as seen in Figure 9. For ZnO A and ZnO A-N_2 (Figure 9 a), the S parameter starts at about 0.54 at the surface and gradually decreases with depth, stabilizing around 0.52, indicating a higher surface electron density that diminishes with penetration depth. A similar trend is observed for ZnO B (Figure 9 c), where the S parameter decreases from 0.52 at the surface to stabilize near 0.50. This enhancement reflects a higher annihilation probability with low-momentum electrons, consistent with a denser population of surface defects or free carriers. ZnO A-Air exhibits a decreased S parameter, indicating electron depletion at the surface after thermal treatment under air. These PAS trends align

with TRPL and TREPR data, reinforcing the correlation between surface defect density and photocatalytic activity, as discussed in the next section 3.2.

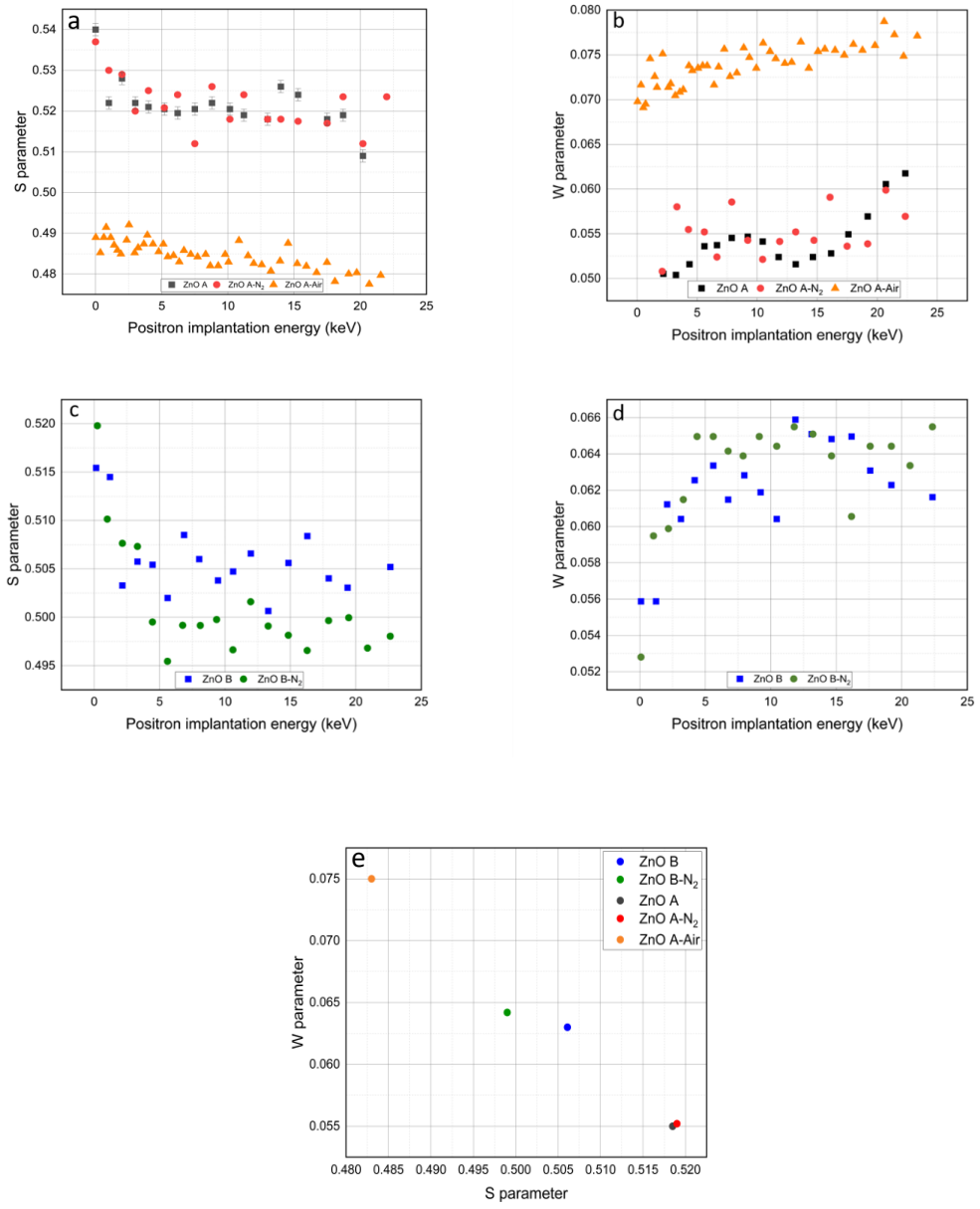

Figure 9 - Positron annihilation spectra with S and W parameters for ZnO A, ZnO A-N_2 and ZnO A-Air (a, b) and for ZnO B and ZnO B-N_2 (c, d), with positron implantation energies up to 20 keV corresponding to a probing depth of about 1 µm. Finally, the S–W correlation (e)

3.2 Photocatalytic results and mechanism of catalytic solvent reduction

Table 2 - Degradation results (triplicate) for all the samples at a photocatalyst concentration of 10 g/L, PNP concentration of 10^{-4} M and 24 h of reaction.

	Adsorption	Photolysis	ZnO A	ZnO A-N_2	ZnO B	ZnO B-N_2	ZnO A-Air	ZnO C	ZnO C-N_2
PNP	No	No	30% ± 2%	65% ± 3%	15% ± 2%	50% ± 3%	10% ± 2%	6% ± 2%	11% ± 2%
IBU	No	No	20% ± 2%	44% ± 3%	8% ± 2%	29% ± 2%	7% ± 2%	5% ± 2%	10% ± 2%

Photocatalytic degradation of *p*-nitrophenol (PNP) under visible light (λ > 395 nm) reveals a strong dependence on the solvent used during synthesis and the post-synthesis annealing atmosphere. Under identical reaction conditions (PNP 10^{-4} M, ZnO dosage 10 g/L, 24 h irradiation), degradation efficiencies varied between 10% and 65%. Such a range cannot arise from differences in morphology or crystallinity alone, but rather reflects distinct defect landscapes that control charge carrier dynamics-particularly the lifetime and availability of valence-band holes. Consistent trends were also observed for ibuprofen degradation under identical conditions (Table 2), confirming the generality of the solvent- and atmosphere-dependent photocatalytic behavior. Since hydroxyl radicals (HO•), the main oxidative agents in PNP degradation [1,20], are formed via hole-mediated processes (eq 4), the persistence of photogenerated holes is the key determinant of photocatalytic efficiency.

$$h^+ + H_2O \rightarrow HO\bullet + H^+ \quad (4)$$

To experimentally identify the dominant reactive species under visible light, scavenger experiments were performed using ZnO A-N_2 as a representative sample, as shown on Figure 10. The addition of isopropanol (HO• scavenger) or ammonium oxalate (AO, h^+ scavenger) led to a pronounced suppression of PNP degradation, demonstrating that hydroxyl radicals and photogenerated holes dominate the oxidation process. This result is fully consistent with the extended hole lifetimes measured by TRPL for ZnO A-N_2.

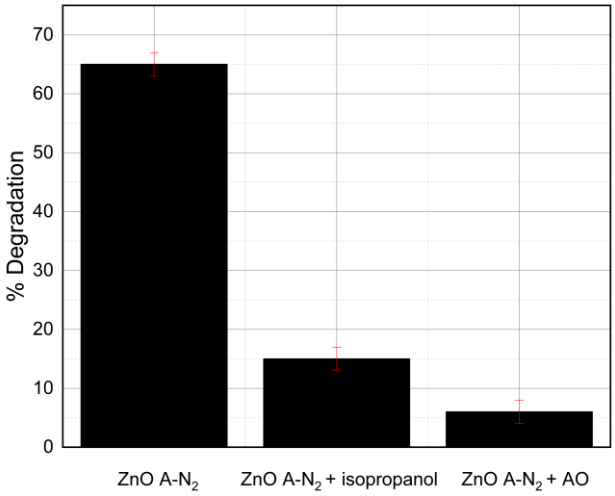

Figure 10 - Photocatalytic degradation of p-nitrophenol (PNP) under visible-light irradiation (λ > 395 nm) over ZnO A-N_2, ZnO A-N_2 with isopropanol (•OH scavenger) and ZnO A-N_2 with ammonium oxalate (hole scavenger)

To complement the degradation efficiencies reported in Table 2, Figure 11 presents the kinetic analysis of PNP degradation under visible-light irradiation, expressed as $\ln(C_o/C)$ as a function of irradiation time. For all samples, a linear dependence is observed, indicating that the degradation follows pseudo-first-order kinetics with respect to PNP concentration. The apparent rate constants extracted from the linear fits increase in the order ZnO B < ZnO A < ZnO B-N_2 < ZnO A-N_2, in full agreement with both the concentration-time profiles and the final degradation efficiencies. Notably, ZnO A-N_2 exhibits the highest reaction rate ($k = 0.042\ h^{-1}$), confirming the beneficial role of methanol-assisted defect formation during N_2 annealing in enhancing visible-light photocatalytic activity.

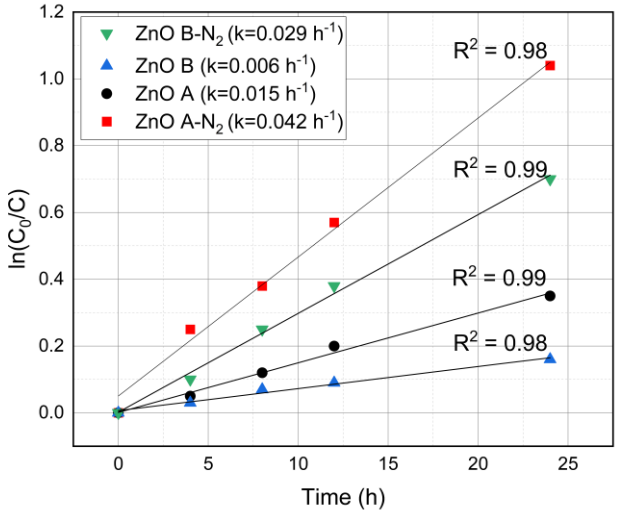

Figure 11 - Pseudo-first-order kinetic plots for the photocatalytic degradation of p-nitrophenol (PNP) under visible-light irradiation (λ > 395 nm) over ZnO A, ZnO A-N_2, ZnO B and ZnO B-N_2.

The comparison between water-, ethanol- and methanol-derived ZnO further clarifies the role of solvent-assisted defect formation during N_2 annealing. For water-derived ZnO, N_2 annealing mainly improves crystallinity, resulting in a modest enhancement of photocatalytic activity, while no significant paramagnetic defects are detected by EPR. In the case of ethanol-derived ZnO, annealing under N_2 does not actively generate new defects but rather stabilizes pre-existing oxygen vacancies by preventing their annihilation and modifying the surface environment, leading to a moderate activity increase. In contrast, methanol-derived ZnO undergoes solvent-assisted surface reduction during N_2 annealing, where residual methanol decomposes on the ZnO surface to generate hydrogenated species that actively promote the formation of zinc vacancies. This distinction explains the markedly superior photocatalytic performance of ZnO A-N_2 compared to ethanol- and water-derived samples.

ZnO synthesized in methanol (ZnO A) clearly outperforms its ethanol-derived counterpart (ZnO B), achieving 30% degradation of PNP in its as-prepared form, compared to only 15% for ZnO B. The superior activity of ZnO A originates from the dual role of methanol, acting both as a synthesis medium and as a reactive precursor. Its higher dielectric constant (ε = 32.6 vs 22.4 for ethanol) promotes slower nucleation and a higher zeta potential (ζ = 22 mV vs 9 mV), stabilizing surface-bound intermediates

and favoring defect retention [1,15,23]. EPR spectra confirm the photoresponsive nature of these defects in ZnO A, with a light-induced signal at *g* = 1.96, characteristic of singly ionized oxygen vacancies (V_O^+), increasing fivefold upon 447 nm excitation. This indicates the presence of traps that are readily activated by visible light. Complementary time-resolved EPR measurements show an electron trapping kinetics slower than ZnO B (k_1 = 70 ms^{-1} and k_3 = 7 ms^{-1} vs ZnO A : k_1 = 25 ms^{-1} and k_3 = 5 ms^{-1}), consistent with a longer availability of the respective charges to find the surface and interact with H_2O, thus showing a better photocatalytic activity than ZnO B. TRPL measurements corroborate this picture: the carrier lifetime (τ_2 = 4.5 ns) reflects a slow recombination component, compared to the time required for the hydroxyl radical to be formed by the interaction between the hole and the water molecule (few ps to ns) [24,25].

Upon annealing ZnO A under nitrogen, the photocatalytic efficiency doubles to 65%, accompanied by the emergence of a persistent EPR signal at *g* = 2.00, attributed to zinc vacancies (V_{Zn}). These defects originate from the catalytic decomposition of methanol on the ZnO surface during annealing. Adsorbed methanol species (Zn-OCH_3) undergo dehydrogenation via surface Zn^{2+}/O^{2-} sites, producing CO and H_2 according to:

$$CH_3OH \rightarrow CO+2H_2 \qquad (5)$$

The hydrogen generated in situ creates a locally reducing atmosphere that partially removes Zn^{2+} from surface sites, yielding zinc vacancies through:

$$ZnO + H_2 \rightarrow ZnO\ (V_{Zn}) + Zn^0 \qquad (6)$$

This mechanism is confined to the top few nanometers, where methanol adsorption and H_2 release occur [26,27]. Given that photocatalysis is a surface-limited process, these surface defects critically influence the observed activity.

These V_{Zn} defects stabilize trapped electrons and extend hole lifetimes, as reflected by the tripling of the slow TRPL component (τ_2 = 11.1 ns) and the grey coloration of ZnO A-N_2. The coexistence of V_O^+-

V_{Zn} thus forms a synergistic defect architecture that enhances charge separation and hydroxyl radical generation. In contrast, air-annealed ZnO A loses this dual-defect network, with reduced TRPL lifetimes (τ_2 = 3.5 ns), attenuated EPR intensity, and a drop in PNP degradation to 10%.

For comparison, ZnO treated with $NaBH_4$ displays the same *g* = 2.00 EPR resonance, confirming that the V_{Zn} centers generated by methanol decomposition are equivalent to those produced by conventional chemical reduction. This validates methanol's role as a self-reducing solvent, capable of promoting vacancy-centered defect formation without external reagents. Ethanol, by contrast, decomposes less readily under the same conditions and primarily generates V_O^+ centers, explaining the weaker photoresponse of ZnO B and its limited visible-light activity.

Together, these findings establish that methanol-derived ZnO uniquely benefits from in situ reductive defect engineering, where solvent decomposition influence surface vacancy formation, charge stabilization, and visible-light photocatalytic efficiency.

4. Conclusion

Our study underscores the pivotal role of solvent-mediated defect engineering in shaping the photocatalytic performance of ZnO. Methanol, unlike ethanol, acts not only as a solvent during synthesis but also as a reactive precursor: during nitrogen annealing at 500 °C, residual methanol decomposes at the ZnO surface, producing CO and H_2 and generating a localized reducing atmosphere that favors the selective formation of zinc vacancies (V_{Zn}). This dual role enables the creation of a compact V_O^+-V_{Zn} defect landscape that is absent in ethanol-derived ZnO.

This approach provides a flexible framework in which parameters such as drying conditions could, in principle, be used to influence residual solvent content and defect formation. As demonstrated here, ZnO A-N_2 exhibits a nearly threefold increase in carrier lifetime (τ_2 = 11.1 ns compared to 4.5 ns for pristine ZnO A), while EPR confirms the emergence of a persistent g = 2.00 signal corresponding to V_{Zn}. These structural modifications translate directly into function: ZnO A–N_2 achieves 65% degradation of p-nitrophenol under visible-light irradiation (λ > 395 nm), compared to only 15% for as-prepared ethanol-derived ZnO B. In contrast, air-annealed ZnO A loses most of its activity (10% degradation), highlighting the essential role of preserving vacancy-type defects.

TREPR kinetics further reveal that electron trapping is slowed in ZnO A-N_2 (k_1 = 25 ms^{-1}, k_2 = 5 ms^{-1}), enhancing hole persistence and promoting hydroxyl radical generation. PAS measurements confirm that the synergistic spatial arrangement of V_O^+ and V_{Zn} defects, rather than the absolute defect density (S-parameter 0.52-0.54), governs the efficiency of charge separation.

Overall, this solvent-driven, dopant-free strategy provides a scalable route to engineer dual-defect architectures, precisely tuning charge-carrier dynamics to optimize visible-light photocatalysis. The approach demonstrates a new paradigm for designing oxide semiconductors with controlled surface defects for solar-driven applications, and shows that subtle control over solvent retention and thermal treatment can double or triple photocatalytic efficiencies compared to conventional synthesis routes.

5. References

[1] A. Farcy, S.D. Lambert, D. Poelman, Z. Yang, F. Drault, S. Hermans, P. Drogui, B. Heinrichs, C. Malherbe, G. Eppe, A. Verdin, J.G. Mahy, Influence of crystallographic facet orientations of sol-gel ZnO on the photocatalytic degradation of p-nitrophenol in water, J Solgel Sci Technol (2024). https://doi.org/10.1007/s10971-023-06301-9.

[2] M. Wang, Y. Zhou, Y. Zhang, E. Jung Kim, S. Hong Hahn, S. Gie Seong, Near-infrared photoluminescence from ZnO, Appl Phys Lett 100 (2012). https://doi.org/10.1063/1.3692584.

[3] C.T. Altaf, O. Coskun, A. Kumtepe, A.M. Rostas, I. Iatsunskyi, E. Coy, E. Erdem, M. Sankir, N.D. Sankir, Photo-supercapacitors based on nanoscaled ZnO, Sci Rep 12 (2022). https://doi.org/10.1038/s41598-022-15180-z.

[4] N. Mediouni, C. Guillard, F. Dappozze, L. Khrouz, S. Parola, C. Colbeau-Justin, A.B.H. Amara, H. Ben Rhaiem, N. Jaffrezic-Renault, P. Namour, Impact of structural defects on the photocatalytic properties of ZnO, Journal of Hazardous Materials Advances 6 (2022) 100081. https://doi.org/10.1016/j.hazadv.2022.100081.

[5] H. Teterycz, O. Rac, P. Suchorska-Woźniak, THE FORMATION MECHANISM OF COLLOIDAL SPHERES OF ZnO IN ETHYLENE GLYCOL, Dig J Nanomater Biostruct 8 (2013) 1157–1167.

[6] R. Rusdi, A.A. Rahman, N.S. Mohamed, N. Kamarudin, N. Kamarulzaman, Preparation and band gap energies of ZnO nanotubes, nanorods and spherical nanostructures, Powder Technol 210 (2011) 18–22. https://doi.org/10.1016/j.powtec.2011.02.005.

[7] E. Rokhsat, A. Khayatian, Enhanced photocatalytic activity of fe doped ZnO hierarchical nanosheets on the degradation of p-nitrophenol under visible light, Inorganic and Nano-Metal Chemistry 48 (2018) 203–209. https://doi.org/10.1080/24701556.2018.1505908.

[8] S.K.S. Parashar, B.S. Murty, S. Repp, S. Weber, E. Erdem, Investigation of intrinsic defects in core-shell structured ZnO nanocrystals, in: J Appl Phys, 2012. https://doi.org/10.1063/1.4725478.

[9] N.M. Flores, U. Pal, R. Galeazzi, A. Sandoval, Effects of morphology, surface area, and defect content on the photocatalytic dye degradation performance of ZnO nanostructures, RSC Adv 4 (2014) 41099–41110. https://doi.org/10.1039/c4ra04522j.

[10] J. Fang, H. Fan, Y. Ma, Z. Wang, Q. Chang, Surface defects control for ZnO nanorods synthesized by quenching and their anti-recombination in photocatalysis, Appl Surf Sci 332 (2015) 47–54. https://doi.org/10.1016/j.apsusc.2015.01.139.

[11] J. Fang, H. Fan, Y. Ma, Z. Wang, Q. Chang, Surface defects control for ZnO nanorods synthesized by quenching and their anti-recombination in photocatalysis, Appl Surf Sci 332 (2015) 47–54. https://doi.org/10.1016/j.apsusc.2015.01.139.

[12] F. Kayaci, S. Vempati, I. Donmez, N. Biyikli, T. Uyar, Role of zinc interstitials and oxygen vacancies of ZnO in photocatalysis: A bottom-up approach to control defect density, Nanoscale 6 (2014) 10224–10234. https://doi.org/10.1039/c4nr01887g.

[13] V. Gurylev, T.P. Perng, Defect engineering of ZnO: Review on oxygen and zinc vacancies, J Eur Ceram Soc 41 (2021) 4977–4996. https://doi.org/10.1016/j.jeurceramsoc.2021.03.031.

[14] L. Pan, S. Wang, W. Mi, J. Song, J.J. Zou, L. Wang, X. Zhang, Undoped ZnO abundant with metal vacancies, Nano Energy 9 (2014) 71–79. https://doi.org/10.1016/j.nanoen.2014.06.029.

[15] X.J. Wang, L.S. Vlasenko, S.J. Pearton, W.M. Chen, I.A. Buyanova, Oxygen and zinc vacancies in as-grown ZnO single crystals, J Phys D Appl Phys 42 (2009). https://doi.org/10.1088/0022-3727/42/17/175411.

[16] N. Ohashi, T. Ishigaki, N. Okada, H. Taguchi, I. Sakaguchi, S. Hishita, T. Sekiguchi, H. Haneda, Passivation of active recombination centers in ZNO by hydrogen doping, J Appl Phys 93 (2003) 6386–6392. https://doi.org/10.1063/1.1569034.

[17] Z. Wang, C. Luo, W. Anwand, A. Wagner, M. Butterling, M.A. Rahman, M.R. Phillips, C. Ton-That, M. Younas, S. Su, F.C.C. Ling, Vacancy cluster in ZnO films grown by pulsed laser deposition, Sci Rep 9 (2019). https://doi.org/10.1038/s41598-019-40029-3.

[18] J.G. Mahy, S.D. Lambert, R.G. Tilkin, C. Wolfs, D. Poelman, F. Devred, E.M. Gaigneaux, S. Douven, Ambient temperature ZrO2-doped TiO2 crystalline photocatalysts: Highly efficient powders and films for water depollution, Mater Today Energy 13 (2019) 312–322. https://doi.org/10.1016/j.mtener.2019.06.010.

[19] J.G. Mahy, C.A. Paez, C. Carcel, C. Bied, A.S. Tatton, C. Damblon, B. Heinrichs, M. Wong Chi Man, S.D. Lambert, Porphyrin-based hybrid silica-titania as a visible-light photocatalyst, J Photochem Photobiol A Chem 373 (2019) 66–76. https://doi.org/10.1016/j.jphotochem.2019.01.001.

[20] A. Farcy, J.G. Mahy, C. Alié, J. Caucheteux, D. Poelman, Z. Yang, P. Eloy, N. Body, S. Hermans, B. Heinrichs, S.D. Lambert, Kinetic study of p-nitrophenol degradation with zinc oxide nanoparticles prepared by sol–gel methods, J Photochem Photobiol A Chem 456 (2024). https://doi.org/10.1016/j.jphotochem.2024.115804.

[21] S.C. Ke, T.C. Wang, M.S. Wong, N.O. Gopal, Low temperature kinetics and energetics of the electron and hole traps in irradiated TiO2 nanoparticles as revealed by EPR spectroscopy, Journal of Physical Chemistry B 110 (2006) 11628–11634. https://doi.org/10.1021/jp0612578.

[22] J. Schultz, R. Lynn, Interaction of positron beams with surfaces, thin films, and interfaces, Rev. Mod. Phys. 60, 701 (1988).

[23] W.-Y. Chen, J.-S. Chen, J.-S. Jeng, Suppression of Oxygen Vacancy and Enhancement in Bias Stress Stability of High-Mobility ZnO Thin-Film Transistors with N 2 O Plasma Treated MgO Gate Dielectrics , ECS Journal of Solid State Science and Technology 2 (2013) P287–P291. https://doi.org/10.1149/2.001307jss.

[24] Y. Nosaka, A. Nosaka, Understanding Hydroxyl Radical (•OH) Generation Processes in Photocatalysis, ACS Energy Lett 1 (2016) 356–359. https://doi.org/10.1021/acsenergylett.6b00174.

[25] S. Sroiraya, W. Triampo, P. Morales, D. Triampo, Ceramic Processing Research Kinetics and mechanism of hydroxyl radical formation studied via electron spin resonance for photocatalytic nanocrystalline titania: Effect of particle size distri-bution, concentration, and agglomeration, 2007.

[26] C.T. Vo, L.K. Huynh, J.Y. Hung, J.C. Jiang, Methanol adsorption and decomposition on ZnO (10 1^{-} 0) surface: A density functional theory study, Appl Surf Sci 280 (2013) 219–224. https://doi.org/10.1016/j.apsusc.2013.04.135.

[27] A.W. Grant, J.H. Larsen, C.A. Perez, S. Lehto, M. Schmal, C.T. Campbell, Methanol decomposition on Pt/ZnO(0001)-Zn model catalysts, Journal of Physical Chemistry B 105 (2001) 9273–9279. https://doi.org/10.1021/jp0118928.

Acknowledgments

Julien G. Mahy, Sophie Hermans and Stéphanie D. Lambert thank the F.R.S.-FNRS for their Postdoctoral Researcher position and Research Directors positions, respectively.

S.C. Acknowledges the fund for scientific research flanders (FWO) for infrastructure funding for the EPR instrumentation (I004920N), and the BOF infrastructure funding from the University of Antwerp for purchasing the FLS1000 spectrometer (project FLUORATE, FN543600001). S. C. acknowledge support from the University of Antwerp through the BOF - Research Centre of Excellence CASCH.

Data Availability Statement

The raw/processed data required to reproduce these findings cannot be shared at this time as these data are part of an ongoing study.

Conflict of interest

The authors declare that there is no conflict of interest concerning this work.

Ethical Approval

The authors declare that they have no known competing financial interests or personal relationships that could have appeared to influence the work reported in this paper.

Consent to Participate

All authors agreed to participate to this work.

Consent to Publish

All authors agreed to this version for publication.

Authors Contributions

Antoine Farcy: Conceptualization, Methodology, Investigation, Formal analysis, Writing – original draft Writing – review & editing. Julien G. Mahy: Methodology, Writing – review & editing, Funding

acquisition and project administration. Sofie Cambré: Investigation, Formal analysis, Writing – review & editing. Eduard Fron: Investigation, Formal analysis, Writing – review & editing. Henk Schut: Investigation, Formal analysis, Writing – review & editing. Sophie Hermans: Investigation, Formal analysis, Writing – review & editing. Stéphanie D. Lambert: Methodology, Writing – review & editing, supervision, Funding acquisition and project administration.